ORNL/TM-11253

ornl

OAK RIDGE NATIONAL LABORATORY

MARTIN MARIETTA

Construction and Initial Operation of the Advanced Toroidal Facility

J. F. Lyon

G. L. Bell
J. D. Bell
R. D. Benson
T. S. Bigelow
K. K. Chipley
R. J. Colchin
M. J. Cole
E. C. Crume
J. L. Dunlap
A. C. England
J. C. Glowienka
R. H. Goulding
J. H. Harris
D. L. Hillis
S. Hiroe
L. D. Horton
H. C. Howe
R. C. Isler
T. C. Jernigan
R. L. Johnson
R. A. Langley
M. M. Menon
P. K. Mioduszewski
R. N. Morris
M. Murakami
G. H. Neilson
B. E. Nelson
D. A. Rasmussen
J. A. Rome
M. J. Saltmarsh
P. B. Thompson
M. R. Wade
J. A. White
T. L. White
J. C. Whitson
J. B. Wilgen
W. R. Wing

OPERATED BY
MARTIN MARIETTA ENERGY SYSTEMS, INC.
FOR THE UNITED STATES
DEPARTMENT OF ENERGY

ORNL/TM-11253
Dist. Category UC-426

CONSTRUCTION AND INITIAL OPERATION OF THE ADVANCED TOROIDAL FACILITY

J. F. Lyon

G. L. Bell*
J. D. Bell†
R. D. Benson‡
T. S. Bigelow
K. K. Chipley‡
R. J. Colchin
M. J. Cole‡
E. C. Crume
J. L. Dunlap
A. C. England
J. C. Glowienka
R. H. Goulding
J. H. Harris
D. L. Hillis
S. Hiroe
L. D. Horton
H. C. Howe
R. C. Isler
T. C. Jernigan
R. L. Johnson‡
R. A. Langley
M. M. Menon
P. K. Mioduszewski
R. N. Morris†
M. Murakami
G. H. Neilson
B. E. Nelson‡
D. A. Rasmussen
J. A. Rome
M. J. Saltmarsh
P. B. Thompson‡
M. R. Wade**
J. A. White‡
T. L. White
J. C. Whitson†
J. B. Wilgen
W. R. Wing

Date published: August 1989

*Auburn University, Auburn, Alabama.
†Computing and Telecommunications Division, Martin Marietta Energy Systems, Inc.
‡Engineering Division, Martin Marietta Energy Systems, Inc.
**Georgia Institute of Technology, Atlanta.

Prepared for the
Office of Fusion Energy
Budget Activity No. AT 10 10 15 B

Prepared by the
OAK RIDGE NATIONAL LABORATORY
Oak Ridge, Tennessee 37831
operated by
MARTIN MARIETTA ENERGY SYSTEMS, INC.
for the
U.S. DEPARTMENT OF ENERGY
under contract DE-AC05-84OR21400

CONTENTS

ABSTRACT

The Advanced Toroidal Facility (ATF) torsatron was designed on a physics basis for access to the second stability regime and on an engineering basis for independent fabrication of high-accuracy components. The actual construction, assembly, and initial operation of ATF are compared with the characteristics expected during the design of ATF.

I. INTRODUCTION

The Advanced Toroidal Facility[1] (ATF), shown in Fig. 1, is currently the world's largest stellarator. The main device and heating parameters are listed in Table I. ATF is an $\ell = 2$ torsatron with constant-pitch helical windings and moderate plasma and coil aspect ratios ($A = R_0/\bar{a} = 7.8$ and $A_c = R_0/\bar{r}_c = 4.5$). Here R_0 is the major radius, $\bar{a}$ is the average plasma radius, and $\bar{r}_c$ is the average helical field (HF) winding radius. The main elements of ATF shown in Fig. 1 are the two independent HF windings, the three independent sets of poloidal field coils [the inner, mid-, and outer vertical field (VF) coil sets], the interior vacuum vessel with large side (0.6 m × 0.9 m) and top/bottom (0.5-m diagonal) ports and smaller (0.2-m-diam) inner ports, and the exterior toroidal structural shell. For reference, the mean diameter of the outer VF coils is 5.9 m, and the top-to-bottom height of the mid-VF coils is 1.7 m.

The various physics and engineering issues in the design of the ATF torsatron were discussed in Ref. 1. Now that ATF has been in operation for a year, it is instructive to compare its fabrication, assembly, and initial results with the characteristics expected during the development of the ATF concept. Harris et

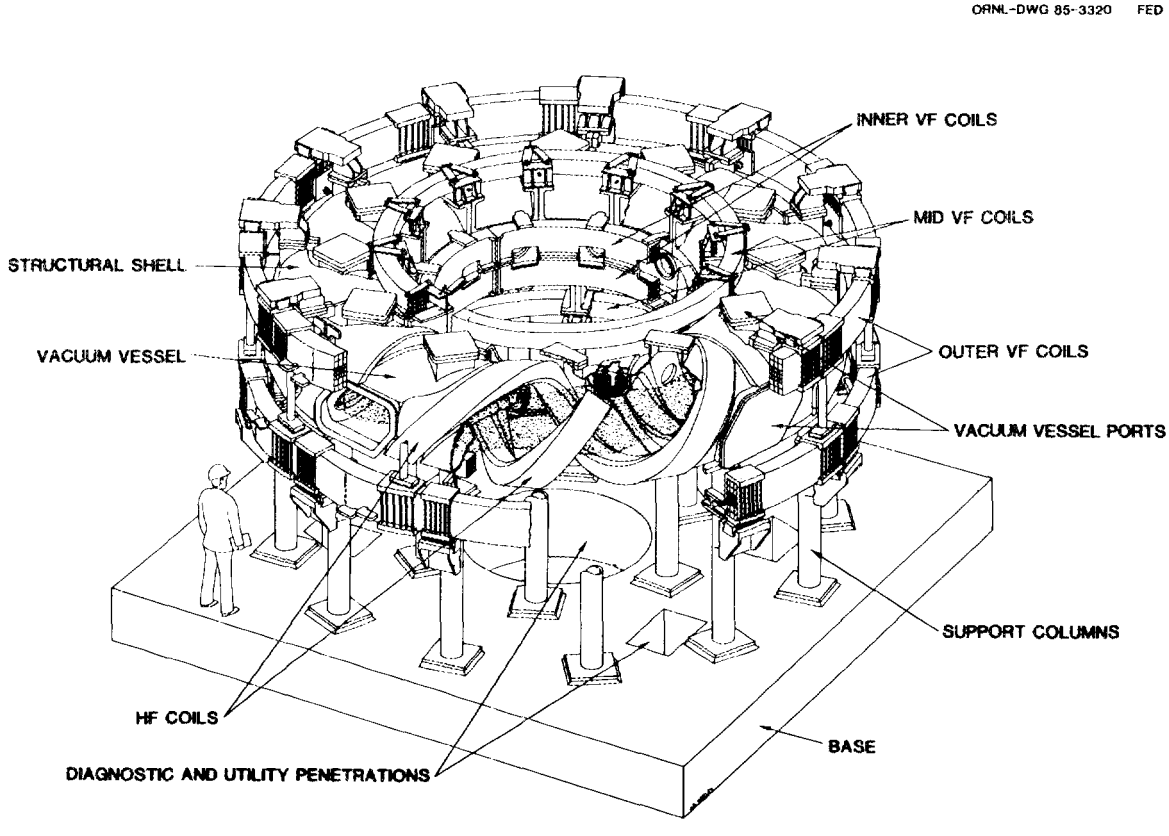

Fig. 1. An artist's sketch of ATF, showing the main components.

Table I. ATF Parameters

Magnetic Configuration	
Poloidal multipolarity, ℓ	2
Number of field periods, M	12
Standard central transform, $\iota(0)$	0.3
Standard edge transform $\iota(\bar{a})$	1.0
Size	
Major radius, R_0	2.1 m
Average minor radius, $\bar{a}$	0.27 m
Plasma volume, V_p	3.0 m^3
Vacuum vessel volume	10.5 m^3
Magnetic Field	
Field on axis, B_0	2 T
Field flattop time	5 s
Plasma Heating[a]	
Electron cyclotron heating	0.4 MW, 53 GHz, steady state (0.2 MW, 53 GHz, 1 s)
Neutral beam injection	3 MW, 40 kV, 0.3 s (1.4 MW, 30 kV, 0.3 s)
Ion cyclotron heating	0.3 MW, 5–30 MHz, 30 s (0.1 MW, 29 MHz, 0.1 s)

[a]Near-term (1989–1990) values; 1988 values in parentheses

al.[2] treat one key feature of ATF, the HF windings and VF coil sets, from this perspective. This article focuses on the overall ATF experience.

II. ATF PHYSICS DESIGN

The key decision in the physics design of ATF was the selection of an HF winding trajectory that produced a magnetic configuration with the potential for high-beta operation. Earlier stellarators had projected beta limits of 1–2%, whereas ATF, with its ability to access a second stability regime directly,[3] was projected to have a volume-average beta limit $\langle\beta\rangle \sim$ 6–8%. The magnetic configuration chosen for ATF is characterized by a rotational transform profile $\iota(r)$ that places the $\iota = \frac{1}{3}$ resonance near the center and the $\iota = 1$ resonance at the edge and by a vacuum central magnetic well that extends out to the $\iota = \frac{1}{2}$ surface. As a result, ATF

occupies a position intermediate between Heliotron E and Wendelstein VII-AS in rotational transform, shear, and magnetic well. The magnetic configurations closest to that of ATF are those of the lower-aspect-ratio Compact Helical System[4] (CHS) and the next-generation Large Helical Device[5] (LHD).

The choice of a medium aspect ratio, $A = 7.8$, for ATF has two potential benefits: a larger plasma radius for approximately the same major radius ($R = 2.1$ m) as Heliotron E and Wendelstein VII-AS and, more importantly, direct access to a higher-beta second stability regime resulting from a self-stabilization effect[6] that occurs with increasing beta. The self-stabilization of curvature-driven instabilities (interchange modes) is caused by the change of the field line curvature (central magnetic well becoming deeper and of larger radial extent) with the increasing outward Shafranov shift of the magnetic axis as beta increases. This effect is larger at lower aspect ratio.

Because of the magnetic hill at the outside (common to all torsatrons), ATF should be unstable to resistive interchange modes in the outer region (shear does not contribute to stabilization of these modes). However, calculations indicate that the extent of the unstable region and the strength of the driving term are reduced by the beta self-stabilization. The net effect expected is an added benefit, a reduction in the anomalous transport associated with resistive pressure-gradient-driven turbulence.[7] ATF was designed to study these effects, with the expectation that values of $\beta_0 \sim 6\%$ would be needed to access the second stability region for the broad pressure profiles ($\beta_0/\langle\beta\rangle = 2.6$) assumed in the design studies.

Figure 2 illustrates how the shift of the magnetic axis and the shape of the pressure profile control access to the second stability regime. For the unshifted case, the beta limit should be set by equilibrium limitations (a large finite-beta axis shift) rather than by a stability limit. An inward shift of the vacuum magnetic axis by more than ~5 cm at low beta should give a relatively low (first stability) beta limit because of the interchange instability. However, it should be possible to operate with the magnetic axis shifted inward by more than ~5 cm (where the confinement properties should be improved because of the effectively lower helical ripple) if the plasma is shifted in after high beta is obtained in the second stability regime (above the knee of the instability boundary in Fig. 2).

The ATF poloidal field coil system was designed to allow access to the second stability regime and to give a large degree of external control over the important vacuum magnetic configuration properties [magnetic axis shift Δ, plasma elongation κ, central rotational transform $\iota(0)$ and global shear, magnetic well depth and extent, magnetic axis topology, etc.]. With the poloidal field system, the net plasma current can be controlled by varying the poloidal flux, the magnetic axis shift and consequently the magnetic well depth by varying the dipole component of the poloidal field, and the elongation of the flux surfaces and the value of $\iota(0)$ by varying the quadrupole component of the poloidal field.[8]

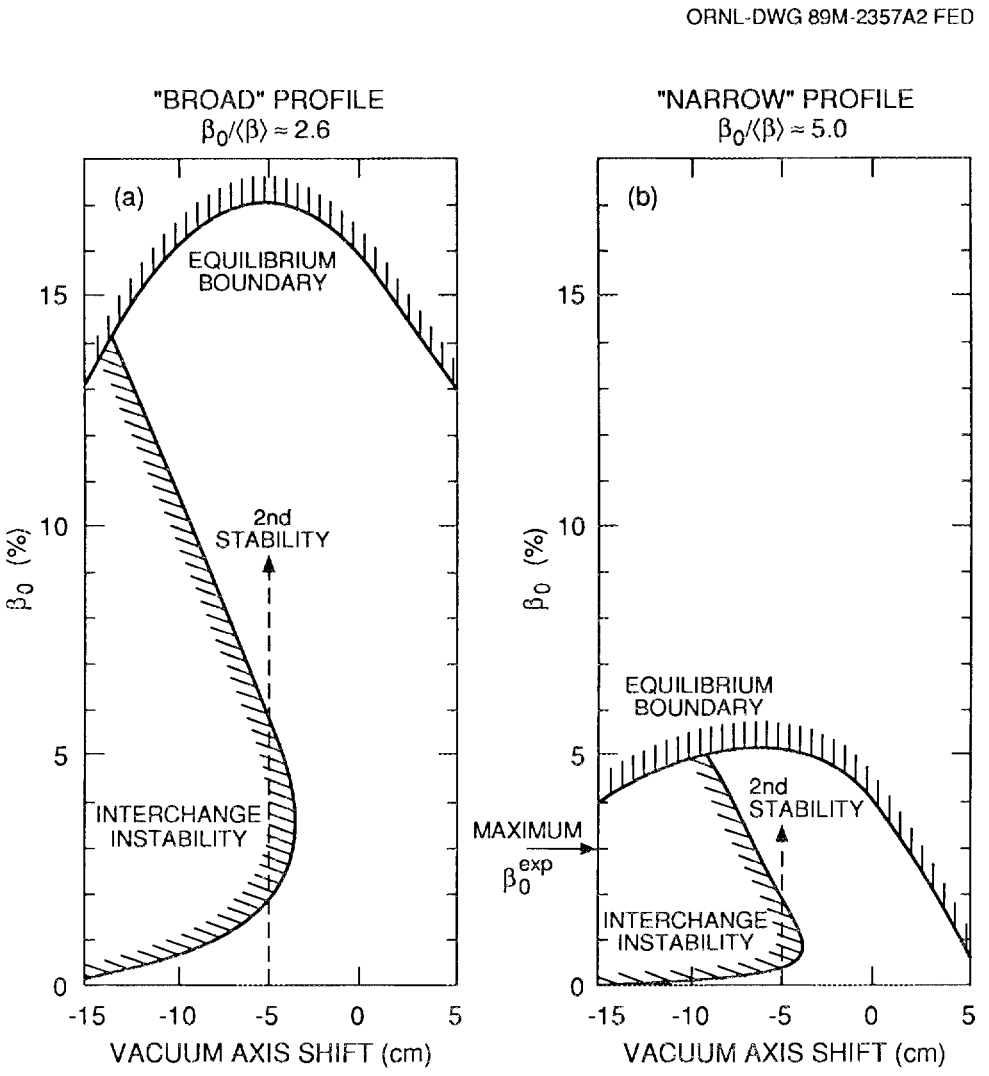

Fig. 2. Second stability region obtained in the standard ATF configuration (a) at high beta for the broad pressure profile assumed in the original design study and (b) at lower beta for the peaked pressure profiles obtained in the 1988 experiments. Beta self-stabilization (stability increasing with increasing beta) occurs for $\beta_0 \sim 4\%$ in (a) and for $\beta_0 \sim 1\%$ in (b).

The vacuum magnetic surfaces (at the $\phi = 0$-deg location where the HF windings cross the midplane) for different axis shifts and plasma shaping are shown in Fig. 3. An inward shift of the vacuum magnetic axis reduces the $\int d\ell/B$ variation on a flux surface and thus should improve the confinement of helically trapped particles, but it also reduces the depth and extent of the central magnetic well (or creates a magnetic hill everywhere). A factor of two reduction in the $\int d\ell/B$ variation on a flux surface can be created by a 10-cm inward shift of the magnetic axis. An

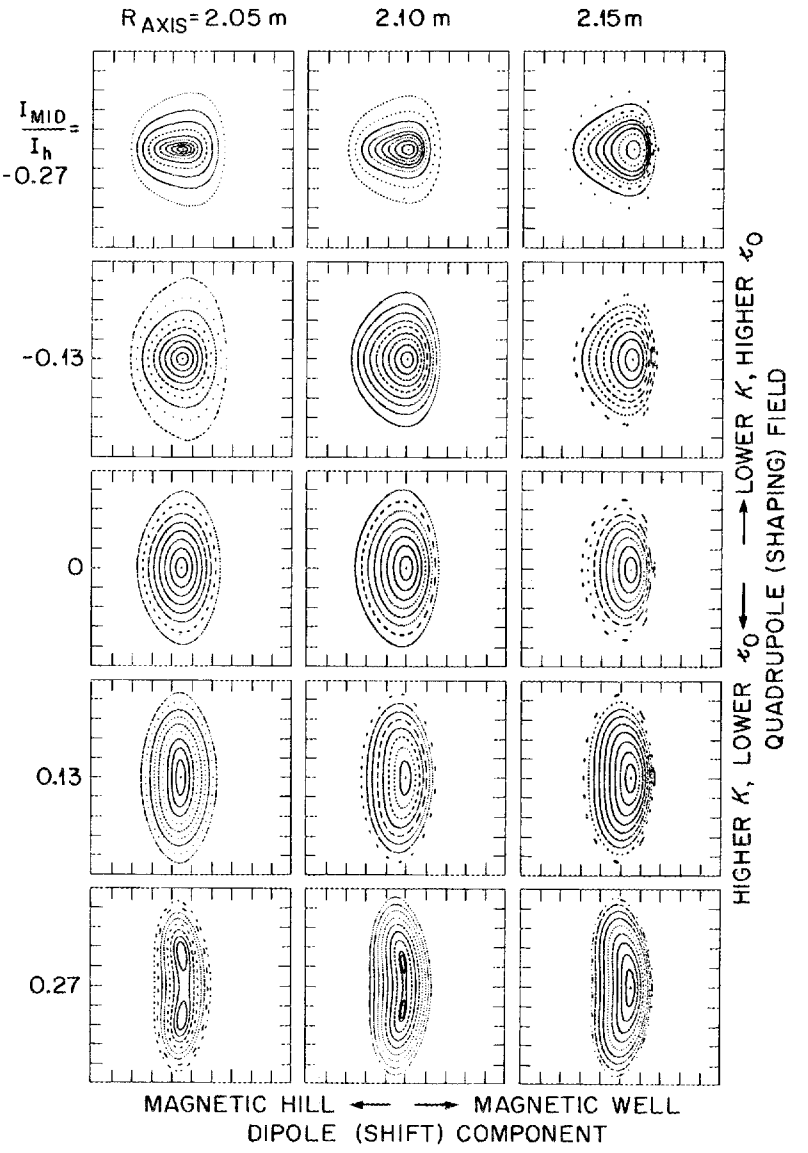

Fig. 3. Vacuum magnetic surfaces at the $\phi = 0$-deg location for different magnetic axis radii and normalized currents in the mid-VF coils (related to the quadrupole component of the field). The standard ATF configuration is in the center of this array; that used most in the 1988 experiments is to the left of it.

outward magnetic axis shift has the opposite effect. Increasing the elongation of the flux surfaces reduces $\iota(0)$ and should allow reduction of the bootstrap current to small values. A low value of $\iota(0)$ leads to an internal separatrix and a bifurcation of the magnetic axis, as shown at the lower left in Fig. 3. Decreasing the elongation has the opposite effect: $\iota(0)$ can be increased above 0.5, and up to 80 kA of bootstrap

current[9] is predicted at low collisionality for $\langle\beta\rangle \simeq 1\%$. Increasing the plasma elongation [decreasing $\iota(0)$] and shifting the magnetic axis inward as beta increases should produce a flux-conserving sequence of equilibria[10] with rotational transform profiles $\iota(\psi)$ essentially the same as the (optimized) vacuum ι profile. Here $2\pi\psi$ is the toroidal flux through a magnetic surface with average rotational transform ι.

III. ATF ENGINEERING DESIGN

The key factor in the engineering design of ATF was the decision to separate fabrication of the vacuum vessel and the HF windings, rather than using a thick vacuum vessel as an accurate winding form for the HF windings as was done in the construction of Heliotron E and CHS. This allows parallel fabrication, faster construction, separate testing of each component, and a less-accurate, thin, one-piece vacuum vessel, but it also requires segmented HF windings with mechanical joints[2,11] and an exterior structural shell. Fabricating the HF windings and the structural shell from pieces that are identical in each field period means that any small perturbations or deviations from the design specifications are the same in each field period and hence amount to a small change in the effective winding law rather than a low-order resonant field error. In addition, individual pieces can be removed and repaired without disassembling an entire system. As part of the research and development (R&D) for the HF segments, a test HF segment was repeatedly assembled from its component pieces, vacuum potted, and disassembled. The ability to remove an HF winding segment was also useful in resolving interferences during installation of the vacuum vessel and the upper HF winding segments.

The exterior toroidal structural shell consists of 24 identical, 4-cm-thick, stainless steel, electrically insulated segments arranged in two toroidal half-shells that are connected by 24 stainless steel side panels, each 5 cm thick. The shell segment and connecting side panels were rough cast or rough formed and machined only where accuracy was required. The relatively small size of the shell segments and side panels simplified the fabrication, finish machining, dimensional checking, and accurate assembly of these pieces (with insulating shims) into the two toroidal half-shells. This design produced no significant difficulties in fabrication or assembly.

The 24 individual, identical HF segments[12] are smaller and hence easier to fabricate and dimensionally check than two complete interlocked HF windings would have been, but full electrical tests had to wait until the HF windings were completely assembled. The bolted joint region is not as strong as the rest of the HF winding and is not as well cooled; this region establishes the operating limits on the current density in the HF winding (3 kA/cm^2 at $B_0 = 2$ T), the pulse length at 2 T (5 s), and the maximum field for steady-state operation (1 T).

The coil systems designed to create the desired magnetic field configurations in ATF are described in Refs. 2 and 11–13. Because large magnetic islands can result from field errors caused by inaccuracies in fabrication or installation of the HF

windings and VF coils, great care was taken with these systems. The completed HF windings are shown preassembled in Fig. 4. The circular VF coils were of standard design and presented no fabrication difficulties other than their large size. A design error in the connections to the HF and VF busbars resulted in the creation of a large ($\simeq$6-cm-wide) magnetic island at the $\iota = \frac{1}{2}$ surface and a nearly continuous series of smaller islands in the outer part of the plasma at low-order rational values of $\iota > \frac{1}{2}$. The busbar connections have since been revised to correct this problem[2] by making the error approximately the same in each field period.

The ATF vacuum vessel,[14] as shown in Fig. 5, is essentially a toroidal shell with helical grooves for the HF windings, contoured to allow vertical removal of the HF winding segments. Both the HF winding cross section and the corresponding trough in the vacuum vessel are chamfered to allow maximum distance between the plasma edge and the vacuum vessel wall.[15] The magnetic loads are transferred to the stainless steel tees on which the HF windings are supported and then to the outer structural shell. There are no radially inward magnetic forces on the HF windings; hence, no support structure is used on the side of the HF windings

ORNL-PHOTO-7828-86

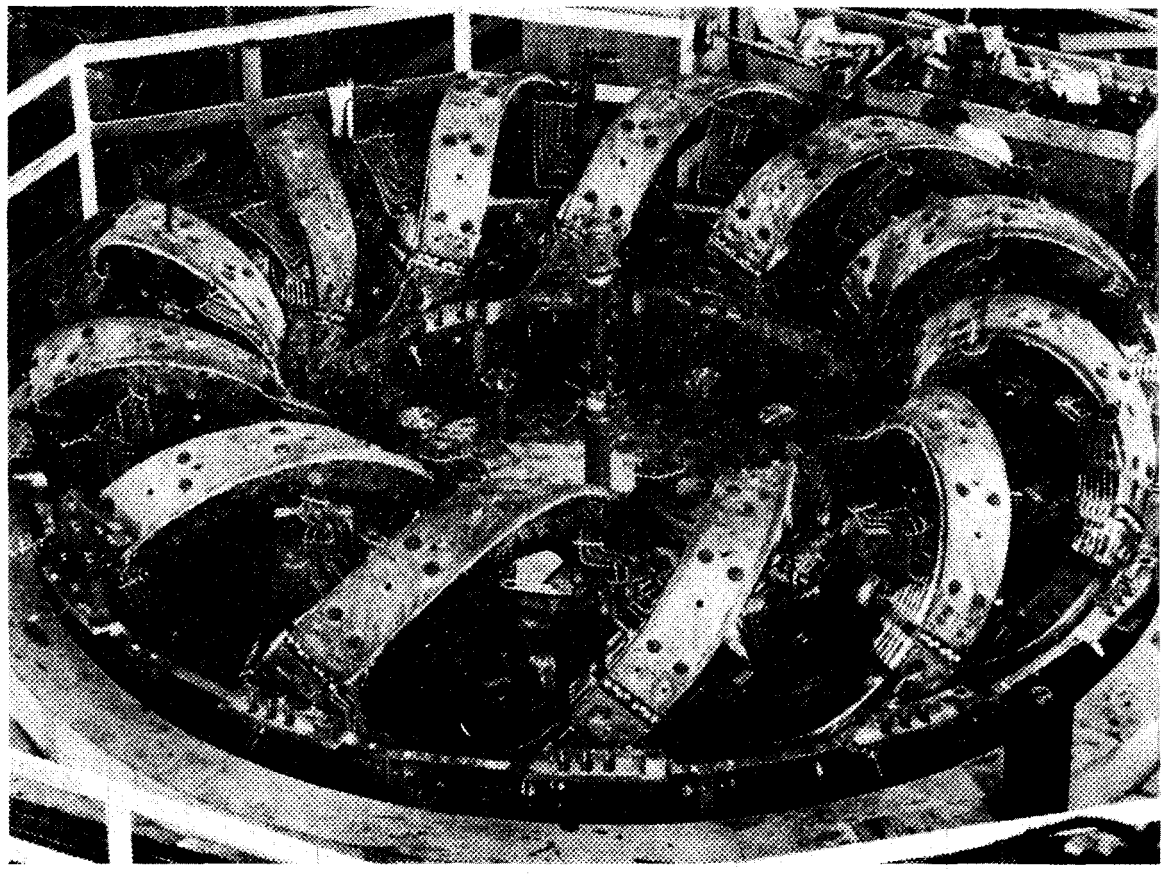

Fig. 4. Completed HF windings for ATF, showing the bolted mechanical joints connecting the top and bottom HF winding segments.

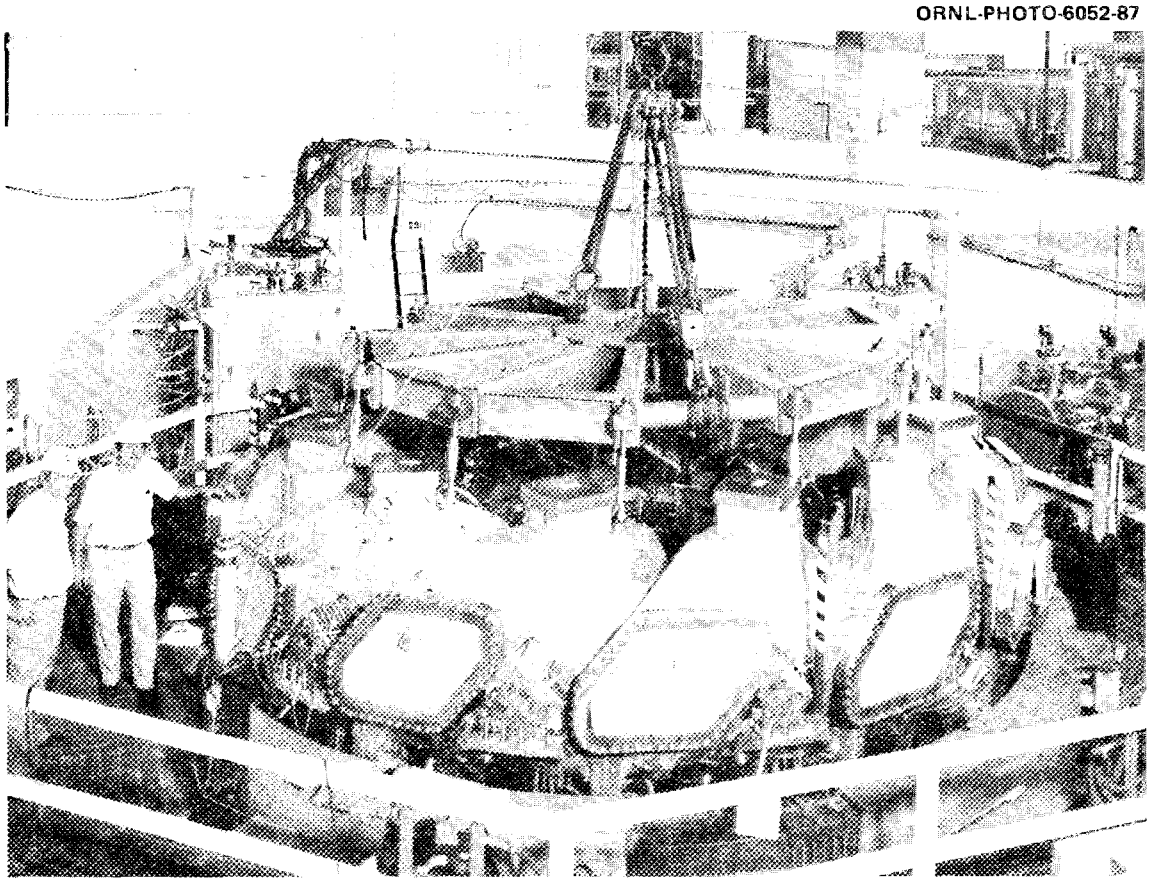

Fig. 5. The ATF vacuum vessel being lowered onto the bottom HF winding segments. The HF segment joints, the helical chamfered groove for the HF winding segments, the large (0.6 × 0.9 m) outside ports, and the square (0.35 × 0.35 m) top ports can be seen.

top and bottom square port locations and expand the vessel to its proper 2.1-m facing the plasma, and the vacuum vessel can be thin (6-mm-thick stainless steel) because the only forces on it are atmospheric and small eddy-current forces. The thin vacuum vessel allows fast (<10-ms) penetration of poloidal fields.

Because there is a nominal 1-cm gap between the outside of the vacuum vessel and the HF windings to allow access to the HF winding joint region and room for a 6-mm radial expansion of the vacuum vessel when it is heated to 150°C, the tolerance on the vacuum vessel fabrication was allowed to be much larger than that used in fabrication of the HF windings. The vacuum vessel fabrication was not an area of concern initially because of this larger tolerance and because the vacuum vessel could be easily modified to meet the design specifications should an error occur, unlike the HF windings, which had to be very accurate because of the difficulty of modifying them.

The original plan[1] was to fabricate the vacuum vessel from ≃400 small sections of stainless steel plate, which would be shaped to the required fit on a precision fixture that formed an internal mold of the vacuum vessel. The forming fixture consisted of 360 steel plates, one each degree toroidally, having the shape of the vacuum vessel interior at that location and mounted on a high-precision base plate. Plans were to tack weld each of the 400 formed plates to its neighbors, cut the large port openings, remove the interior forming plates, and make the interior welds.

However, a series of circumstances led to a vacuum vessel[14] that was out of the required tolerance range. First, 1200, rather than 400, formed plates were used, which required more welding. Second, shrinkage of the ≃1 km of Inconel welds was greater than expected. Third, when the interior forming plates were removed, the vacuum vessel was weakened; this condition was made worse when the outside welds required deeper backgrinding from the inside than expected for good full-penetration welds. These factors led to a 3.8-cm shrinkage of the major radius of the vacuum vessel. The solution was to slot-cut the vacuum vessel every 30° at the major radius. Final cuts and expansion were required at three toroidal locations before the vacuum vessel met all the design specifications. The additional welds for the larger number of vacuum vessel plates and for correction of the vacuum vessel dimensions increased the time necessary for leak checking and repair of small leaks. Also, weld distortion during the correction of the vacuum vessel dimensions led to small offsets in the vacuum vessel flanges that had to be compensated. The net result was an 16-month delay in delivery of the vacuum vessel. In retrospect, it would have been better to make the vacuum vessel in 12 sections, whose accuracy would have been easier to control, and to weld the 12 sections together after accurately positioning them.

Of the 16-month delay, 4 months were recovered through the preassembly and testing allowed by the independent fabrication approach used. All 24 segments of the HF windings were finished before the vacuum vessel was ready, so the HF windings were preassembled as shown in Fig. 4, and their mechanical accuracy and electrical properties were checked. Preassembly of the windings proved that there were no fabrication errors greater than the ±1-mm accuracy needed to avoid an unacceptable level of field errors. The absence of the vacuum vessel allowed access to both the inside and the outside of the joint region during the match drilling of the joints, which greatly simplified this task. The electrical tests allowed us to verify that the joint contact resistances and the total coil resistances were correct as calculated to within a few percent. Preassembly of the structural shell without the vacuum vessel allowed us to account for all machining variations and to calculate, precut, and attach the necessary shims ahead of time. No problems were encountered in preassembly of either the HF windings or the structural shell. The preassembly and testing reduced the time required for final assembly of ATF (after installation of the vacuum vessel) from the expected 7 months to 3 months.

IV. ASSEMBLY OF ATF

Assembly of ATF occurred over a 30-month period beginning in July 1985, when the concrete base was prepared. In March 1986, the lower outer VF coil and the bottom half of the structural shell were in place. From April through September 1986, the lower HF winding segments were assembled and installed. In October 1986, the HF windings were complete. The vacuum vessel was installed in August 1987. In December 1987, the ATF assembly was complete.

Care was taken in all aspects of the device fabrication and assembly to avoid inaccuracies or perturbations that would create field errors. At each stage of the assembly, a computerized optical triangulation system (twin electronic theodolites) with a measurement accuracy of 0.025 mm at a distance of 4.6 m was used to ensure accuracy. The individual components (structural shell segments, HF winding segments) were separately measured with a five-axis computerized coordinate measuring machine that could measure components to an accuracy of 0.025 mm in a volume $2 \times 1 \times 1$ m. The lower half of the structural shell had machined surfaces accurate to 0.25 mm that were used as a measurement reference for the rest of the assembly process. Also, each HF segment was fitted with three optical targets and a spherical seat. The spherical seat precisely matched an adjustable tooling ball that was accurately located in each of the 12 bottom structural shell segments to allow independent positioning of each HF segment.

The major ATF components were assembled[13] in the sequence shown in Fig. 6. The procedure was essentially that outlined in Ref. 1. The first step in assembly was preparation of the 61-cm-thick reinforced concrete pad and the 18 support columns on which the structural shell rests. The reinforcing bars in the concrete pad and the support columns are nonmagnetic stainless steel to avoid magnetic field perturbations that could create magnetic islands at low-order rational values of ι. The lower outer VF coil was set into place and connected through insulated brackets to the support columns in a temporary position. In a similar way, the lower mid-VF coil was positioned and attached to insulated brackets to allow later mounting on the structural shell. The bottom half of the structural shell was then lowered into place and connected through insulating pads to the support columns. Inflatable fiberglass-filled plastic bladders were positioned in each lower shell segment to assist in transferring the normal and toroidal force from each HF segment to the structural shell. Next, each lower HF segment was accurately positioned and secured with structural ties; then its bladder was filled with epoxy.

At this stage, the planned next step was to lower the vacuum vessel into place over the lower HF segments. However, the delay in fabrication of the vacuum vessel described in Sec. III allowed us to preassemble the HF windings and the structural shell, to check their mechanical accuracy and electrical properties, and to take measures that would accelerate the final assembly process. When the vacuum vessel arrived, it was lowered into place as a unit on temporary supports, as shown in Fig. 5. Next, the 12 upper HF winding segments were reinstalled and thermally

Fig. 6. The major ATF components in the assembly order, showing (1) the bottom HF winding segments in the bottom half of structural shell, (2) the vacuum vessel, (3) the top HF winding segments, (4) the side connecting panels, and (5) the top half of the structural shell.

cycled, and the fiberglass-filled plastic bladders were added before the upper half of the structural shell was reinstalled. Measurements showed that all the spherical seats in the top HF segments were within 0.5 mm of their intended positions. Figure 7 shows ATF at this near-final stage of assembly.

The upper half of the structural shell was then lowered into place and bolted to the 24 insulated side panels that were in turn bolted to the bottom half of the structural shell. The ties that connect the upper HF segments to the structural shell were installed, and the plastic bladders were then filled with epoxy to assist in transmitting the HF segment force to the structural shell. The temporary supports for the vacuum vessel were removed, and the vacuum vessel weight was supported

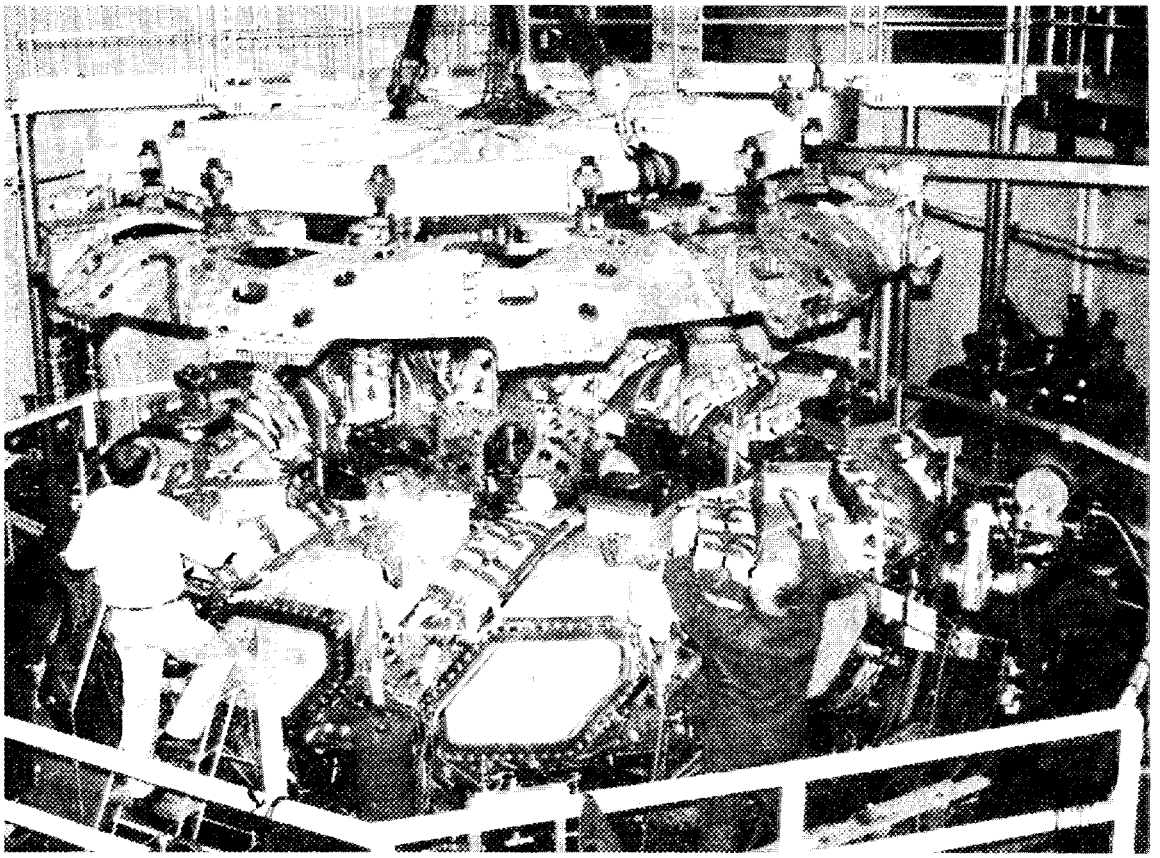

Fig. 7. The ATF assembly after installation of the upper HF winding segments and the force-transmitting fiberglass-filled bladders and before final installation of the top half of the structural shell.

from the upper half of the structural shell on a set of pinned supports, which allow thermal expansion of the vacuum vessel in the radial direction. The lower outer VF coil was raised from its stored position and aligned. The upper outer VF and mid-VF coils were lowered into position and connected to the structural shell through insulated brackets, and insulated adjustable columns were installed between the VF coil pairs to carry the principal VF coil forces. Finally, the inner VF coil set was positioned and attached to the structural shell. The VF coils were positioned radially and vertically to within ± 3 mm of their intended location relative to the HF winding center. This completed the mechanical installation of ATF. The last stage was connecting the utilities to ATF: more than 1000 water cooling connections, the vacuum pumping duct and pumps, and the HF and VF coil leads to the appropriate busbar feeds.

V. PLASMA HEATING AND DIAGNOSTICS

Two important auxiliary systems on ATF are the plasma heating systems and the plasma diagnostics. Some of these systems can be seen in the photograph of the completed ATF in Fig. 8. The three heating systems are electron cyclotron heating (ECH) for currentless plasma startup and electron heating, neutral beam injection (NBI) for bulk plasma heating, and ion cyclotron heating (ICH) for development of long-pulse heating. The main parameters of these systems are given in Table I.

The ECH power is generated by a 200-kW continuous-wave (cw) gyrotron oscillator tube and is coupled to ATF with a 6.35-cm-diam quasi-optical waveguide operating in the TE_{01} or TE_{02} mode. The entire 27-m-long ECH transmission system[16] is evacuated to $\sim 10^{-7}$ Torr. The transmission system includes two TiO_2 noncircular electric mode absorbers, two 90° miter bends with phase-correcting mirrors to reduce mode conversion losses, and a waveguide mode analyzer with a

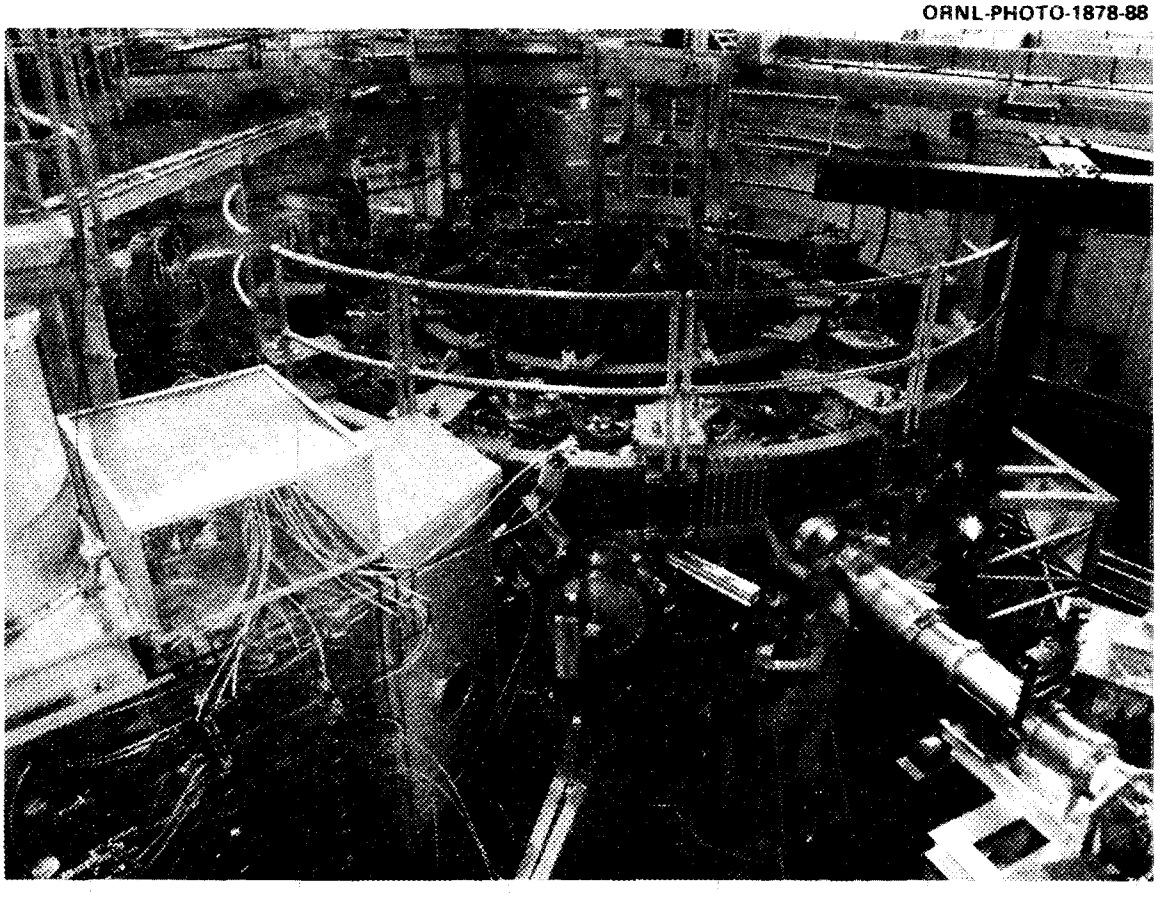

Fig. 8. The completed ATF with some of the major plasma diagnostics and plasma heating systems. The large box at the left is one of the two neutral beam lines.

linear array of rectangular apertures. The overall system efficiency is 87%. When the TE_{02} mode is propagated without intermediate mode conversions (the standard setup in the 1988 experiments), the mode purity falls from 92% at the gyrotron to $\simeq$70% at the launcher because of mode conversion in the two miter bends. A simple open waveguide with a broad, conical, unpolarized radiation pattern (−20-dB beam width of 79 cm with a null on axis at the ATF midplane) operating at the second harmonic and located 1.2 m above the ATF midplane has been used for low-field (top) launch for the 1988 studies. With a TE_{02} to TE_{01} mode converter, the mode purity is 85% TE_{01} at the launcher, mainly because of the gyrotron and not the miter bends, and the radiation pattern is narrower (estimated to be 48 cm at the −20-dB point in the ATF midplane). A polarized directional launcher with a narrower beam width (12 cm at −20 dB) has been used in early 1989 operation to improve the single-pass absorption over that for the open waveguide launcher. With some waveguide cooling, the ECH system is capable of steady-state operation. It has been used for second harmonic heating (B_0 = 0.94 T) at the 200-kW level for 1-s pulses. Fundamental heating at B_0 = 1.9 T, longer pulses, and installation of a second 200-kW system are scheduled for 1989.

The neutral beam lines[17] are those that were used on the Impurity Study Experiment (ISX-B) tokamak with the front ends and apertures modified for the ATF injection geometry.[18] Two neutral beams are aimed tangentially 13 cm inside the standard (R_0 = 2.1 m) magnetic axis to minimize beam scrape-off on the vacuum vessel walls. They are aimed in opposing directions to provide balanced injection for no net momentum input or net beam-driven current. Each duoPIGatron ion source can provide a 100-A, 0.3-s, 40-kV ion beam with a 1.1-deg (HWHM) divergence. The beam species mix (power fractions) at the source is 80% H^+, 15% H_2^+, and 5% H_3^+ at 30 kV. Each beam line can provide 1 MW at 40 kV through the ATF port, 4.1 m from the ion source. During the 1988 run, however, each beam line was used only up to 0.75 MW at 33 kV.

Preliminary tests have started on ATF with an uncooled fast-wave ICH antenna[19] at the 100-kW level. The antenna[19] uses the compact resonant double loop design developed at Oak Ridge National Laboratory that is also used on the Tokamak Fusion Test Reactor (TFTR), Doublet III-D, and Tore Supra. It has a two-tier Faraday shield and a 15-cm radial motion capability. The Faraday shield is bordered by graphite tiles, and the Faraday shield tubes are covered by 3-mm-thick cylindrical graphite tiles. The antenna is shaped to the plasma boundary and is mounted on the outside with the current strap 10 deg counterclockwise from the vertical for the fast-wave studies. The antenna can be reoriented $\simeq$90 deg (with modifications) for ion Bernstein wave heating. It is tunable over the frequency range from 10 to 30 MHz and can provide 1 MW with moderate loading (2 Ω, or 4.6 $\Omega \cdot m^{-1}$ for the 0.43-m long current strap). Antenna loading experiments in hydrogen plasmas were performed at $2\omega_{cH}$ (28.8 MHz) in the 1988 run with the magnetic axis shifted in by 5 cm. The results showed an exponential decrease (with

an e-folding distance of 5 cm) in the plasma loading with increasing separation between the plasma boundary and the current strap. The maximum loading was 0.6–0.77 Ω (1.4–1.8 $\Omega \cdot m^{-1}$) at the minimum separation of $\simeq$12 cm. The loading resistance also increased approximately linearly with density and frequency over the operating range. Thus, operation with the plasma closer to the antenna, which should be possible now that the field errors have been corrected, and at higher density should lead to higher loading and effective heating.

The ATF diagnostics already installed or in preparation are listed in Table II. The main diagnostics are those providing profile (multichord) and multichannel information: (1) the 12 segmented Rogowski coils; (2) the 5 Mirnov loops; (3) the 15-channel far-infrared (FIR) interferometer; (4) the 5-chord H_α monitors; (5) the 7-position bolometers; (6) the 10- and 18-detector soft X-ray arrays; (7) the 20- to 1250-Å grazing incidence spectrometer; (8) the 2000- to 10,000-Å visible

Table II. The ATF Diagnostic Systems

Installed by May 1989	
Rogowski coil	Hard X-ray detectors
Segmented Rogowski coil	Soft X-ray array (Heliotron E)
Diamagnetic loop	Pulse height analyzer
Magnetic (Mirnov) loops	
	Grazing incidence spectrometer
CCD cameras	Visible spectrometer
Vacuum vessel thermocouples	Vacuum Czerny-Turner spectrometer
Residal gas analyzer	Visible bremsstrahlung
2-mm microwave interferometer	2-D Thomson scattering
FIR interferometer	Electron cyclotron emission
8-shot pellet injector	
	Neutral particle analyzer
H_α monitors	Neutron detectors
Bolometers	
Infared cameras	Limiter thermocouples
	Limiter Langmuir probes
	Reciprocating Langmuir probe
Planned for 1989, 1990	
2-D scanning neutral particle analyzer	CO_2 laser scattering
Microwave reflectometer	Edge spectrometer
Laser ablation	Soft X-ray array (ATF)
Bolometer array	Heavy ion beam probe

spectrometer; (9) the 1150- to 8000-Å vacuum Czerny-Turner spectrometer; (10) two-dimensional (2-D) Thomson scattering; (11) the 16-channel electron cyclotron emission (ECE); (12) the 2-D scanning neutral particle analyzer; (13) the fast reciprocating Langmuir probe; (14) the microwave reflectometer; (15) the 12-chord visible bremsstrahlung; (16) the 2000- to 6000-Å edge spectrometer; and (17) the 200-kV heavy ion beam probe.

VI. SUMMARY OF INITIAL ATF OPERATION

The first ATF operating period[20] in January 1988 was chiefly concerned with machine and diagnostic commissioning and with currentless plasma production using 200-kW, 53.2-GHz ECH at 0.95 T. This was followed in March and April 1988 by coil alignment studies and electron-beam mapping of the magnetic surfaces.[2] The coil alignment studies indicated that the HF windings and the VF coil sets were accurately positioned to within 1 mm. However, the magnetic surface mapping indicated a chain of islands extending outward from $r/\bar{a} \simeq 0.6$ with the largest island (6-cm width) at $\iota = \frac{1}{2}$, as shown in Fig. 9. The field errors were later found to be due to uncompensated dipoles at the current feeds to the HF windings and the VF coils.[21]

In the second operating period (May–September 1988), experiments[22] were conducted in the presence of the uncompensated field errors. The plasma was characterized by narrow $T_e(r)$ profiles, as shown in Fig. 10, and there were sharp

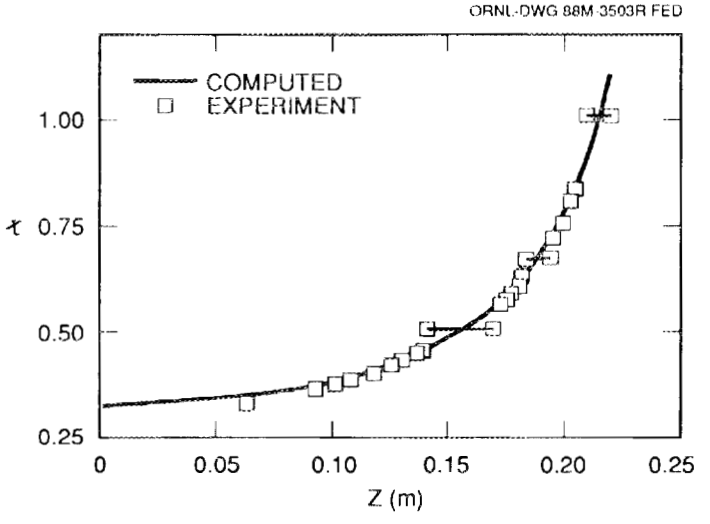

Fig. 9. The rotational transform profile in the vertical (Z) direction in the $\phi = 0$-deg plane for the standard ATF configuration. Magnetic islands (indicated by the horizontal lines connecting equal values of the measured ι) were created by the original connections of the HF windings and VF coils to their busbars. These connections have since been redone.

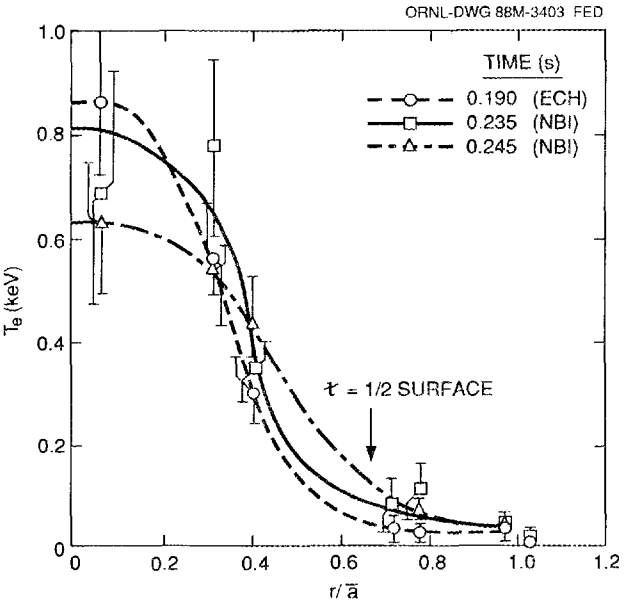

Fig. 10. Peaked electron temperature profiles obtained with both ECH and NBI in ATF, presumably due to the presence of the large magnetic island at $\iota = \frac{1}{2}$ and the string of islands for $\iota > \frac{1}{2}$.

reductions in plasma stored energy W_p and line-averaged density $\bar{n}_e$ for outward magnetic axis shifts, as shown in Fig. 11. The narrow profiles could be modeled[23] by assuming that χ_i and χ_e were neoclassical (including ripple) in the plasma interior but that χ_e was anomalously large for $r/\bar{a} > 0.5$, an indication that the observed island structure was degrading confinement. Error field calculations that accurately modeled the amplitude and phase of the magnetic islands also showed that the extent of these islands grew as the magnetic axis was shifted outside $R_0 = 2.1$ m. The combination of the decreasing radius of the $\iota = \frac{1}{2}$ surface and the growth of the magnetic island at $\iota = \frac{1}{2}$, shown in Fig. 12, led to the best plasma performance being obtained at $R_0 = 2.05$ m, 5 cm inside the nominal axis position, as shown in Fig. 11.

Despite the deterioration associated with the chain of magnetic islands for $\iota \geq \frac{1}{2}$, the global ATF confinement is consistent with the LHD scaling[5] when the nominal full radius ($\bar{a} = 0.27$ m) is used to calculate this scaling value for ATF, as shown in Fig. 13 (from Ref. 5). The confinement times τ_E in ATF (indicated by the shaded areas) also decrease with neutral beam power, in agreement with the LHD scaling. The uncompensated field errors did not seem to have a major effect on the geometry of the diverted flux outside the nominal last closed flux surface. Langmuir probe measurements of the particle flux in the divertor stripe show a narrow (2-cm) peak.[24]

An effect of the narrow pressure profiles was that second stability behavior was obtained at values of β_0 less than half that anticipated for the broader (nominal)

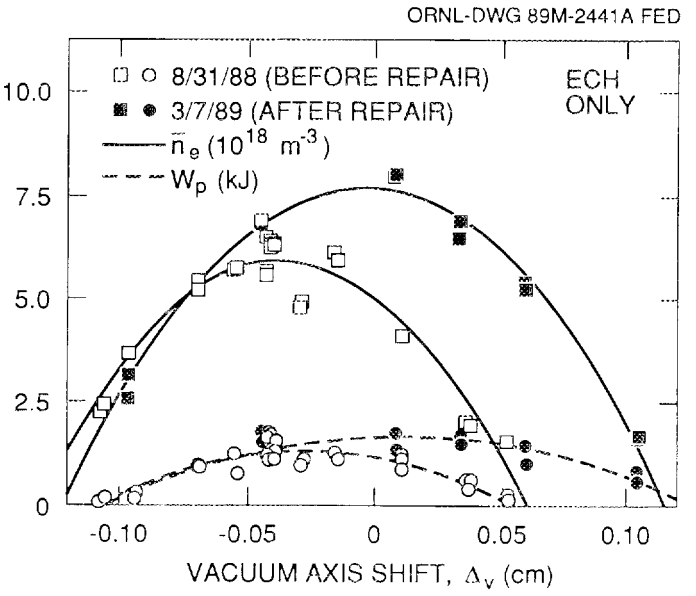

Fig. 11. Stored energy (dashed curves) and central line-averaged density (solid curves) before and after the field error correction. A wider operational range (outward shift of the magnetic axis) is obtained after the field error correction.

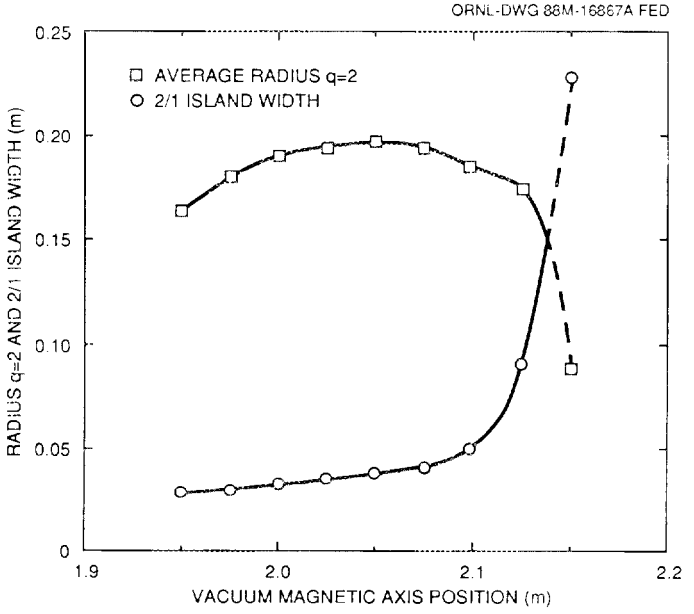

Fig. 12. Before the field error correction, the space available between the magnetic axis and the edge of the $\iota = \frac{1}{2}$ island, the difference between the two solid curves shown, decreased rapidly for magnetic axis positions outside $R_0 = 2.1$ m, the standard (design) axis position.

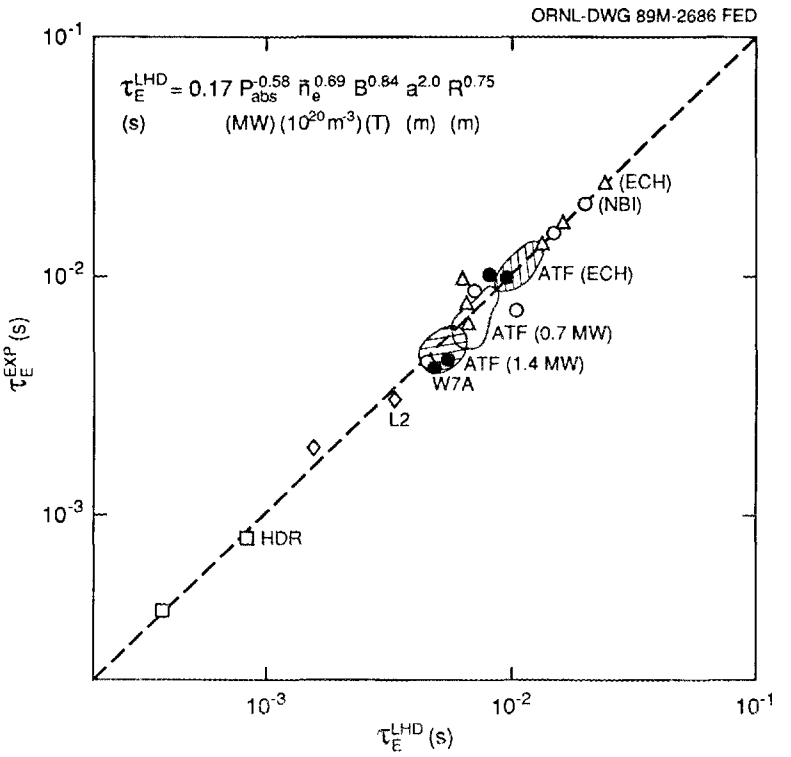

Fig. 13. Global energy confinement times in ATF and in other stellarators vs a scaling expression used in the LHD design studies. The nominal full ATF radius ($\bar{a} = 27$ cm) is used in the calculation of τ_E, and the shaded areas indicate ATF data obtained with 0.2-MW ECH, 0.7-MW NBI, and 1.4-MW NBI.

profiles.[25,26] In effect, the narrow profiles reduced the edge value of ι to $\frac{1}{2}$ and increased the plasma aspect ratio by a factor ~ 1.6. This led to a larger Shafranov shift of the magnetic axis ($\Delta/\bar{a} \simeq \beta_0\ A/\iota_{edge}^2$) and to a greater deepening of the magnetic well than was anticipated. Experimental evidence for the beta self-stabilization effect on ATF is shown in Fig. 14. The amplitude of the coherent part[26] of the $n = 1$ fluctuations in the 8- to 40-kHz range, observed on Mirnov loops separated by 180 deg toroidally, is shown as a function of beta. The envelope of the maximum value of the coherent fluctuations first rises with beta and then starts to fall for $\langle\beta\rangle \gtrsim 0.25\%$. If beta self-stabilization were not occurring, then the fluctuation amplitude should have continued to increase with beta, especially since the axis shift moves the plasma closer to the loops at higher beta. The experimental β_0 values obtained (up to 3%) are well above the theoretically predicted transition ($\beta_0 \simeq 1.3\%$) to the second stability regime for the observed profiles. Time-dependent magnetic fluctuation data show a beta dependence during a single shot similar to that seen in Fig. 14. The measured fluctuations are consistent with theoretical predictions for resistive pressure-gradient-driven interchange modes.[26]

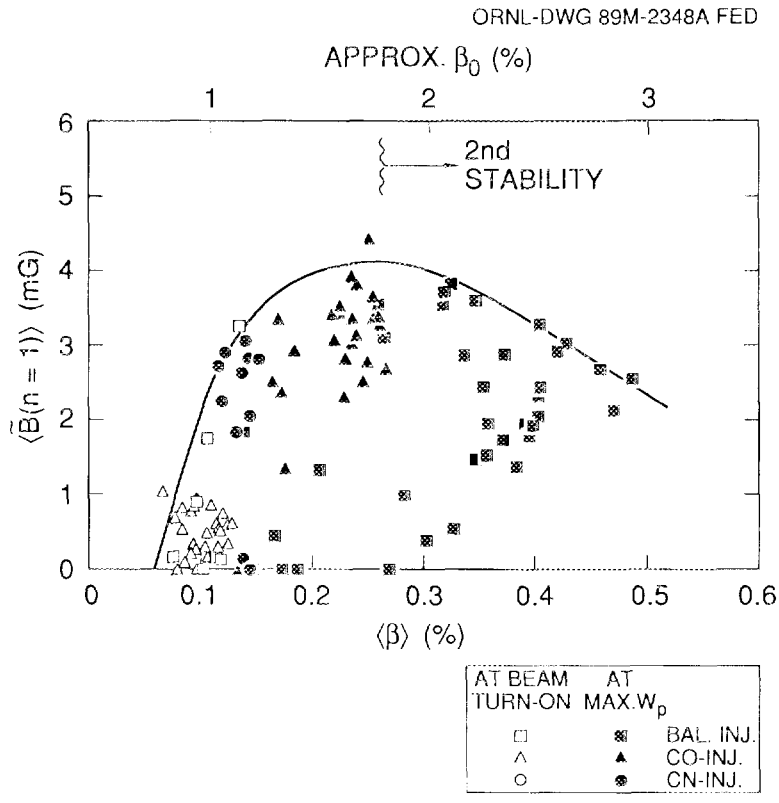

Fig. 14. Variation of the maximum amplitude of coherent $n = 1$ magnetic oscillations with increasing beta, indicating a beta self-stabilization effect and entrance to a second stability regime.

Additional evidence for beta self-stabilization is obtained from the broadening of the pressure profile with increasing beta, as shown in Fig. 15. The data points give a profile broadness factor $\langle\beta\rangle\bar{n}_e T_{e0}^{\mathrm{ECE}}$ for co-, counter-, and balanced injection when the neutral beam is turned on and at the peak of the stored energy. This broadness factor has been benchmarked with Thomson scattering profiles and $\nabla T_e(r)$ from the ECE measurements. The beta dependence of the broadness parameter is similar to the theoretical expansion of the magnetic well region ($V'' < 0$) with increasing beta, as shown by the dashed curve in Fig. 15. Other possible causes of profile broadening do not correlate as well with the profile broadening as does beta. A sequence of MHD stability calculations using pressure profiles that broaden with beta, as found experimentally, shows that the plasma remains marginally stable along the path to the second stability regime.

Figure 16 shows some of the best data obtained in the May–September 1988 experimental period. Balanced (co- plus counter-injected) H^0 neutral beams (1.4 MW total) were injected tangentially into a hydrogen plasma at $B_0 = 0.95$ T. The magnetic axis was located at $R_0 = 2.05$ m. Chromium gettering of about

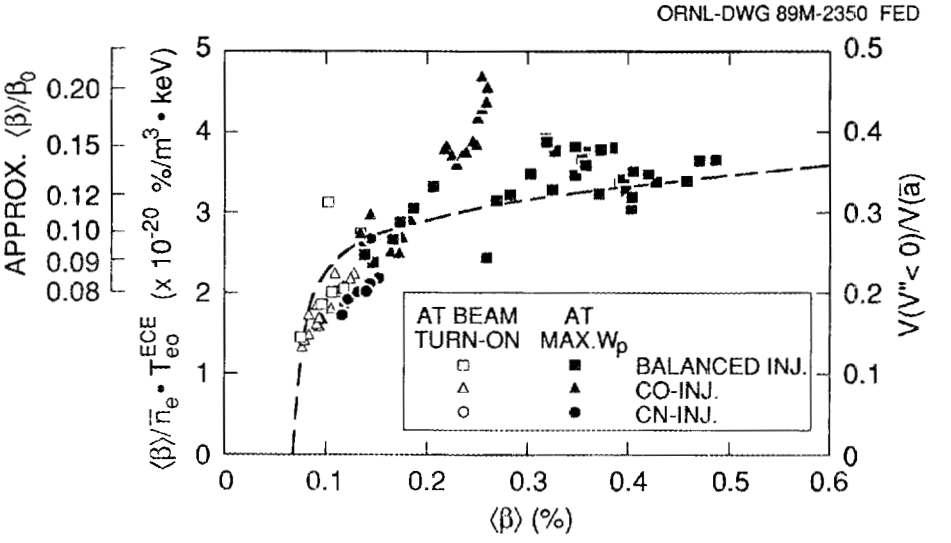

Fig. 15. Measures of profile width indicate that the pressure profile broadens as beta increases, in agreement with the expectations of the beta self-stabilization effect. The dashed curve shows that the fraction of the plasma volume inside the magnetic well $\left[\text{volume}(V'' < 0)/\text{volume}(\bar{a})\right]$ is calculated to increase with beta.

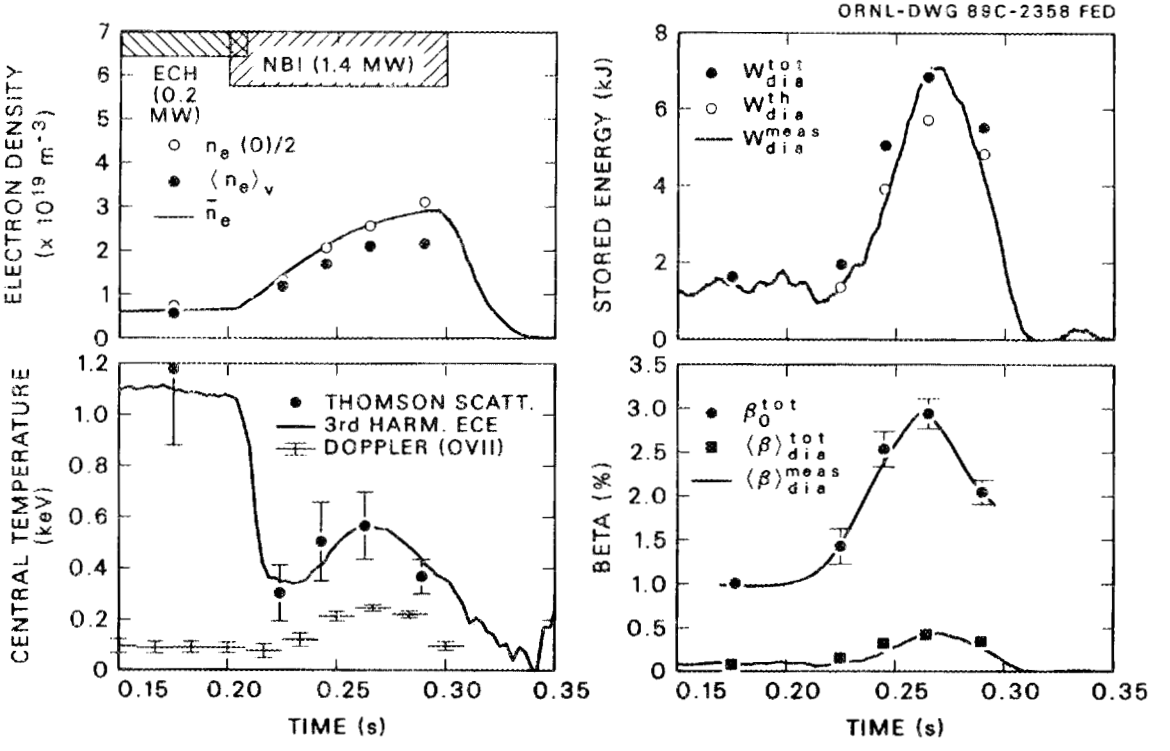

Fig. 16. ATF data obtained at $B_0 = 0.95$ T during the 1988 experimental operation.

one-third of the vacuum vessel surface was used for this case, resulting in a Z_{eff} between 1.5 and 2. The plasma parameters at $t = 0.265$ s (the peak of the plasma stored energy) were $\bar{n}_e = 2.5 \times 10^{19}$ m^{-3}, $n_e(0) \simeq 5 \times 10^{19}$ m^{-3}, $T_e(0) \simeq 0.6$ keV, $T_i(0) \simeq 0.26$ keV, $W_p \simeq 7$ kJ, $\langle\beta\rangle \simeq 0.5\%$, $\beta(0) \simeq 3\%$, and $\tau_E \simeq 5$ ms. Higher values for $T_e(0)$ ($\simeq$1 keV at lower density) and for τ_E ($\simeq$15 ms) are obtained in discharges heated only by ECH.

Small net plasma currents are obtained in ATF. The plasma current for the discharge shown in Fig. 16 was less than 1 kA, but higher plasma currents (up to $\simeq$6 kA) can be obtained with unbalanced tangential NBI. The plasma current during NBI is probably driven mostly by the neutral beam. The noninductive plasma current during the ECH period (probably bootstrap current) is larger than 1 kA because it must overcome a small negative loop voltage (-0.1 V to -0.2 V) due to a transient in the HF winding current.

Because of its complex topology and the complicated manufacturing procedure, the vacuum vessel has been plagued with high leak rates. Before installation, the leak rate was an acceptable 1×10^{-5} Torr $\cdot$ ℓ/s. After one year of operation, with diagnostics and other appendages installed, the global leak rate had increased by an order of magnitude. This is most likely a consequence of stresses induced by thermal cycling. The effect of the leak on the plasma impurity content is to some extent alleviated by chromium gettering, leading to typical oxygen concentrations near 1%. We are presently investigating options for solving the leak problem.

Various wall cleanup procedures were tried in the 1988 experimental period.[27] Electron cyclotron resonance (2.45-GHz) discharge cleaning at $B_0 = 0.88$ kG and glow discharge cleaning alone were not effective. The ECH plasmas exhibited uncontrollable density increases, eventually approaching cutoff and 100% radiated power, then collapsing to a low-density, low-temperature afterglow plasma. However, within two weeks after a major vacuum opening, simultaneous glow discharge cleaning and baking of the vacuum vessel and its major extensions to temperatures between 70°C and 140°C allowed essentially steady-state (1-s) ECH plasma operation, as shown in Fig. 17. The rate of rise of n_e after the initial breakdown indicates the cleanliness of the plasma. Both spectroscopy and visible bremsstrahlung indicated that Z_{eff} was in the range from 1.5 to 2 during both ECH and NBI operation.

However, NBI-heated plasmas continue to show the collapse phenomenon[28] noted in early ECH discharges. In the typical NBI-heated discharge shown in Fig. 18, the plasma stored energy rises rapidly after the start of the neutral beam pulse but then falls, followed later by a rapid decrease in the plasma density. This collapse can be simulated by modeling with the PROCTR code[29] for narrow $T_e(r)$ profiles under the assumption that χ_e and χ_i are neoclassical in the center but that χ_e is anomalously large outside $r/\bar{a} \simeq 0.5$. The narrow $T_e(r)$ profile allows low ionization stages to penetrate the outer plasma region, resulting in a large radiating volume. The results of the PROCTR code indicate that the combination of the narrow $T_e(r)$ profile and the observed factor of two rise in the impurity influx during

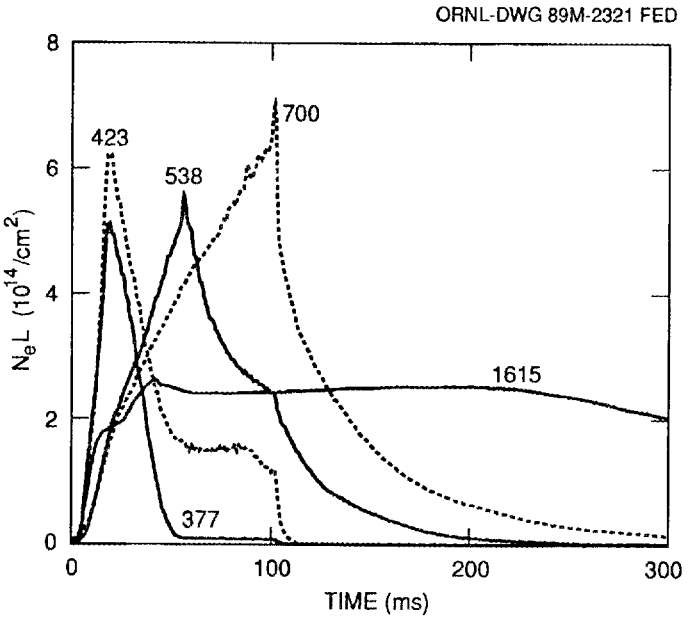

Fig. 17. Central line-averaged density history in ATF, indicating the progress of wall cleanup. The labels are ATF shot numbers.

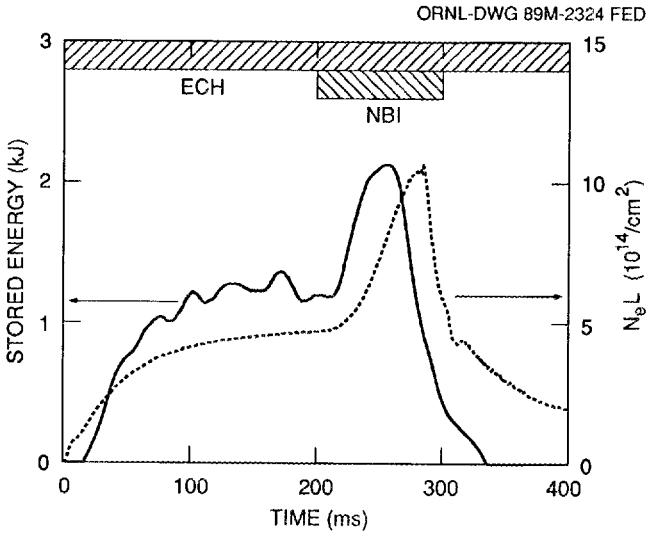

Fig. 18. Collapse of density (central line integral) and stored energy during an NBI-heated discharge in ATF.

NBI is theoretically sufficient to initiate the thermal collapse, but this point has not been conclusively demonstrated by experiments. Spectroscopic measurements[30] suggest that impurity radiation may drive the collapse but the development of strong poloidal asymmetries in the emission is an important feature. The stored energy peaks $\simeq$60 ms after injection begins, when $Z_{eff} \simeq 2$ and $P_{rad}/P_{abs} \simeq 0.37$.

The electron density continues to rise, because of fueling from the neutral beams and the influx of cold gas from the beam lines. The edge radiation rises and the electron temperature falls as the density rises. When T_e falls below $\simeq$100 eV, the plasma becomes radiatively unstable and P_{rad}/P_{abs} rises to $\simeq$100% while the density collapses.

During the October–December 1988 period, the VF coil connections were modified and compensating current loops were installed in the HF coil system to correct the earlier field errors. The magnetic surfaces were mapped again with the electron-beam probe.[2] The magnitude of the $\iota = \frac{1}{2}$ island dropped from $\simeq$6 cm to $\simeq$1 cm at $B_0 \simeq 1$ T and scaled inversely with the square root of the helical field strength. This indicates that the small residual field error causing the present $\iota = \frac{1}{2}$ island arises from a constant resonant stray field component ($\sim$0.1 G, smaller than the ambient magnetic field) and not from inaccurate coil alignment or uncompensated dipoles in the bus work. The islands outside the $\iota = \frac{1}{2}$ surface also decreased in size, but those inside $\iota = \frac{1}{2}$ increased. All observed islands now decrease with increasing B, indicating that the bulk of the field perturbation responsible for the islands is not inherent in the magnetic field coils, except for the island at $\iota = \frac{1}{3}$, which is independent of B. The $\iota = \frac{1}{3}$ island should not have a significant effect because it is in the plasma interior and can be avoided by raising $\iota(0)$ above $\frac{1}{3}$; however, its cause is not known at present.

Preliminary operation (March 1989) after repair of the field error indicates that the $T_e(r)$ profiles are broader,[31] although the central values are not as high, as shown in Fig. 19, and that a broader range of vacuum axis shifts (toward the outside) is available, as shown in Fig. 11. Profile analysis for the same heating power (0.7-MW unbalanced NBI) gives $\beta_0/\langle\beta\rangle$ = 3–4 vs $\beta_0/\langle\beta\rangle$ = 5–7 before the repairs. Long-pulse ECH operation has been recovered with chromium gettering, although better control is still needed. The stored energy in NBI-heated plasmas now remains high for a longer time before the eventual collapse occurs. However, much more work needs to be done in learning to operate ATF in the most effective manner.

VII. CONCLUSIONS AND NEAR-TERM STUDIES

ATF was designed from an engineering viewpoint to take advantage of parallel fabrication of small, high-accuracy parts that were then assembled into larger components and from a physics viewpoint to access a higher-beta second stability regime. In general, the engineering design strategy was successful. The critical components that would have been difficult to modify (the HF winding segments) met all the design specifications. The less accurate vacuum vessel suffered from some fabrication problems, but the independent parallel fabrication of the other ATF components minimized the impact of the vacuum vessel delay on final assembly of ATF. Unanticipated dipoles (current loops) in the HF and VF bus feeds led to field errors (now corrected) that created a large island at the $\iota = \frac{1}{2}$ surface and a string

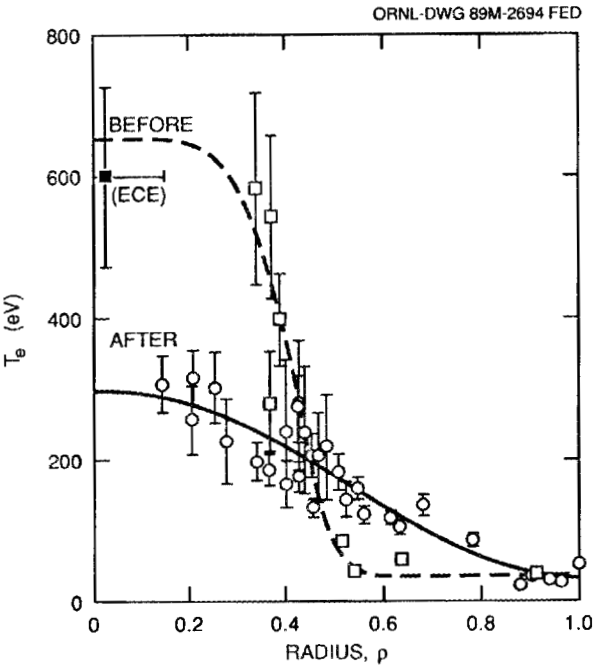

Fig. 19. Electron temperature profiles from Thomson scattering before (dashed curve and square points) and after (solid curve and round points) the field error correction, obtained with unbalanced NBI.

of islands for $\epsilon > \frac{1}{2}$. This resulted in peaked pressure profiles and a lower-beta access to the second stability regime due to an exaggerated Shafranov shift of the magnetic axis. The main ATF systems have been commissioned, and most of the remaining systems (principally some diagnostics) should be in full operation by mid-1989. The ATF program for the next few years will be directed toward vindication of the physics design of ATF. A good beginning has been made, with some indications of second stability behavior, and ATF is now functioning as designed, but the bulk of the work is ahead.

A number of additions are planned for ATF through 1990. ATF has operated routinely (for $\simeq$5500 shots) at 1 T and began operation at 2 T in May 1989. This is expected to improve performance because of the B dependence of τ_E, the higher efficiency of ECH at the electron cyclotron fundamental resonance, and the reduced beta (and effects associated with it). An 8-shot pellet injector installed in May 1989 should allow central fueling and peaking of the density profile. An additional 200-kW, 53.2-GHz gyrotron will be added (doubling the ECH power to 400 kW), and the ICH power will be increased from 100 kW to 300 kW. The mid-VF coil power supply will be connected, allowing control of the plasma ellipticity and the value of $\epsilon(0)$. A number of diagnostics will be added (fast reciprocating Langmuir probe, 15-channel FIR interferometer, 2-D scanning neutral particle analyzer, microwave reflectometer, 200-kV heavy ion beam probe, etc.), and more getters will be added

to cover $\simeq$60% of the vacuum vessel wall (vs $\simeq$30% at present). Titanium gettering may also be used to allow more density control during NBI. The emphasis of the physics studies on ATF during 1989 will be better understanding of confinement through correlation of fluctuations with local transport coefficients and comparison with theory.

ACKNOWLEDGMENT

The authors acknowledge the encouragement of O. B. Morgan, M. W. Rosenthal, and J. Sheffield of Oak Ridge National Laboratory.

REFERENCES

1. J.F. LYON, B.A. CARRERAS, K.K. CHIPLEY, M.J. COLE, J.H. HARRIS, et al., "The Advanced Toroidal Facility," *Fusion Technol.*, **10**, 179 (1986).
2. J.H. HARRIS, T.C. JERNIGAN, F.S.B. ANDERSON, R.D. BENSON, R.J. COLCHIN, M.J. COLE, A.C. ENGLAND, et al., "Realization of the ATF Torsatron Magnetic Field," *Fusion Technol.*, accepted for publication (1989).
3. B.A. CARRERAS, H.R. HICKS, J.A. HOLMES, V.E. LYNCH, L. GARCIA, J.H. HARRIS, T.C. HENDER, and B.F. MASDEN, "Equilibrium and Stability Properties of High-Beta Torsatrons," *Phys. Fluids*, **26**, 3569 (1983).
4. M. FUJIWARA, K. MATSUOKA, K. YAMAZAKI, K. NISHIMURA, T. AMANO, T. KAMIMURA, H. SANUKI, J. TODOROKI, and Y. ABE, "Design Studies on Compact Helical Systems," *Proc. Int. Stellarator/Heliotron Workshop*, Kyoto, Japan, November 1986, Vol. I, p. 288, PPLK-5, Kyoto University, Kyoto (1987); K. NISHIMURA, K. MATSUOKA, M. FUJIWARA, K. YAMAZAKI, J. TODOROKI, T. KAMIMURA, et al., "CHS Physics and Engineering Design," in this issue.
5. DESIGN GROUP FOR THE NEW LARGE HELICAL SYSTEM DEVICE, "New Large Helical System Device—Outline," unpublished (1988); A. IIYOSHI et al., "The Large Helical Device Project," *Fusion Technol.*, accepted for publication (1989).
6. L.M. KOVRIZHNYKH and S.V. SHCHEPETOV, "MHD Equilibrium and Stability of Stellarator Plasma," *Nucl. Fusion*, **23**, 859 (1983).
7. B.A. CARRERAS, "Anomalous Transport in the Second Stability Regime," *Comments Plasma Phys. Controlled Fusion*, **12**, 35 (1988).
8. G.H. NEILSON and J.H. HARRIS, "Harmonic Analysis for Magnetic Configuration Control in Experimental Stellarator Devices," *Nucl. Fusion*, **27**, 711 (1987).
9. K.C. SHAING, B.A. CARRERAS, E.C. CRUME, N. DOMINGUEZ, S.P. HIRSHMAN, V.E. LYNCH, and W.I. VAN RIJ, "Bootstrap Current Control and the Effects of the Radial Electric Field in Stellarators," *Proc. 7th Int. Workshop on Stellarators*, Oak Ridge, Tennessee, April 1989, to be published by International Atomic Energy Agency, Vienna (1989).
10. B.A. CARRERAS, H.R. HICKS, J.A. HOLMES, V.E. LYNCH, and G.H. NEILSON, "Zero-Current High-Beta Stellarator Equilibria with Rotational Transform Profile Control," *Nucl. Fusion*, **24**, 1347 (1984).
11. B.E. NELSON, W.E. BRYAN, F.L. GORANSON, and J.E. WARWICK, "Mechanical Testing and Development of the Helical Coil Joint for the Advanced Toroidal Facility," *Proc. 11th Symp. Fusion Engineering*, Austin, Texas, November 1985, Vol. 1, p. 418, Institute of Electrical and Electronics Engineers, New York (1985).
12. M.J. COLE, J.C. WHITSON, and B.J. BANKS, "Fabrication of the Helical Field Coil Components for the Advanced Toroidal Facility," *Proc. 12th*

Symp. Fusion Engineering, Monterey, California, 1987, Vol. 1, p. 21, Institute of Electrical and Electronics Engineers, New York (1988).

13. B.E. NELSON, "Final Assembly and Initial Operation of the Advanced Toroidal Facility," *Proc. 15th Symp. Fusion Technology*, Utrecht, The Netherlands, September 1988, Vol. 1, p. 391, North-Holland, Amsterdam (1989).
14. K.K. CHIPLEY and G.N. FREY, "Fabrication and Installation of the Vacuum Vessel for the Advanced Toroidal Facility," *Proc. 12th Symp. Fusion Engineering*, Monterey, California, November 1987, Vol. 1, p. 217, Institute of Electrical and Electronics Engineers, New York (1988).
15. J.F. LYON, J.A. ROME, and R.H. FOWLER, "Particles and Field Lines Outside the ATF Plasma," *J. Nucl. Mater.*, **121**, 415 (1984).
16. T.L. WHITE, T.S. BIGELOW, and H.D. KIMREY, Jr., "Initial High-Power Testing of the ATF ECH System," *Proc. Sixth Joint Workshop on Electron Cyclotron Emission and Electron Cyclotron Resonance Heating*, Oxford, England, September 1987, p. 377, Culham Laboratory, Abingdon, England (1987).
17. M.M. MENON, R.N. MORRIS, and P.H. EDMONDS, "ATF Neutral Beam Injection System," *Proc. 11th Symp. Fusion Engineering*, Austin, Texas, November 1985, Vol. 2, p. 1269, Institute of Electrical and Electronics Engineers, New York (1986).
18. R.N. MORRIS, R.H. FOWLER, J.A. ROME, and T.J. SCHLAGEL, "Advanced Toroidal Facility Neutral Beam Injection: Optimization of Beam Alignment and Aperturing," *Fusion Technol.*, **12**, 281 (1987).
19. F.W. BAITY, D.J. HOFFMAN, and T.L. OWENS, "ICRF Heating on ATF," *AIP Conf. Proc.*, **129**, 32 (1985).
20. G.H. NEILSON, F.S.B. ANDERSON, D.B. BATCHELOR, G.L. BELL, J.D. BELL, T.S. BIGELOW, et al., "Currentless Plasma Generation and Heating in the ATF Torsatron," *Proc. 15th European Conf. Controlled Fusion and Plasma Physics*, Dubrovnik, Yugoslavia, May 1988, Vol. 12B, Part II, p. 486, European Physical Society (1988).
21. R.J. COLCHIN, J.H. HARRIS, F.S.B. ANDERSON, A.C. ENGLAND, R.F. GANDY, J.D. HANSON, et al., "Correction of Field Errors in the ATF Torsatron," *Proc. 16th European Conf. Controlled Fusion and Plasma Physics*, Venice, Italy, May 1989, Vol. 13B, Part II, p. 615, European Physical Society (1989).
22. M.J. SALTMARSH, F.S.B. ANDERSON, G.L. BELL, J.D. BELL, T.S. BIGELOW, M.D. CARTER, et al., "Initial Experimental Results from the ATF Torsatron," *Proc. 12th Int. Conf. Plasma Physics and Controlled Nuclear Fusion Research*, Nice, France, 1988, paper IAEA CN-50/C-1-2, to be published by International Atomic Energy Agency, Vienna (1989).

23. H.C. HOWE, L.D. HORTON, E.C. CRUME, J.H. HARRIS, R.C. ISLER, J.B. WILGEN, and W.R. WING, "Transport Modeling of ECH and Neutral-Beam-Heated Plasmas in the Advanced Toroidal Facility," *Proc. 16th European Conf. Controlled Fusion and Plasma Physics*, Venice, Italy, March 1989, Vol. 13B, Part II, p. 683, European Physical Society (1989).
24. P.K. MIODUSZEWSKI, T. UCKAN, D.L. HILLIS, J.A. ROME, R.H. FOWLER, J.C. GLOWIENKA, M. MURAKAMI, and G.H. NEILSON, "Edge Plasma and Divertor Studies in the ATF Torsatron," *Proc. 16th European Conf. Controlled Fusion and Plasma Physics*, Venice, Italy, March 1989, Vol. 13B, Part II, p. 623, European Physical Society (1989).
25. M. MURAKAMI, B.A. CARRERAS, J.H. HARRIS, F.S.B. ANDERSON, G.L. BELL, J.D. BELL, et al., "Second Stability Studies in the ATF Torsatron," *Proc. 16th European Conf. Controlled Fusion and Plasma Physics*, Venice, Italy, March 1989, Vol. 13B, Part II, p. 575, European Physical Society (1989); also published as ORNL/TM-11138, Oak Ridge National Laboratory (1989).
26. J.H. HARRIS, M. MURAKAMI, B.A. CARRERAS, J.D. BELL, G.L. BELL, T.S. BIGELOW, et al., "Second Stability in the ATF Torsatron," submitted to *Phys. Rev. Lett.* (1989).
27. R.C. ISLER, E.C. CRUME, L.D. HORTON, H.C. HOWE, and G.S. VORONOV, "Spectroscopic Studies of Plasma Collapse in the Advanced Toroidal Facility," *Nucl. Fusion* (in press).
28. R.C. ISLER, L.D. HORTON, G.S. VORONOV, E.C. CRUME, G.L. BELL, R.F. GANDY, et al., "Temperature Behavior During Neutral-Beam Injection in a Torsatron (ATF) with Field Errors," *Nucl. Fusion* (in press).
29. H.C. HOWE, "Physics Models in the Tokamak Transport Code PROCTR," ORNL/TM-9537, Oak Ridge National Laboratory (1985).
30. R.C. ISLER, L.D. HORTON, E.C. CRUME, H.C. HOWE, and G.S. VORONOV, "Impurity Studies in the Advanced Toroidal Facility," *Proc. 16th European Conf. Controlled Fusion and Plasma Physics*, Venice, Italy, March 1989, Vol. 13B, Part II, p. 619, European Physical Society (1989).
31. D.A. RASMUSSEN, A.C. ENGLAND, M. MURAKAMI, H.C. HOWE, T.L. CLARK, R.R. KINDSFATHER, et al., "Recent Electron Temperature and Density Results from the ATF Thomson Scattering System," *Proc. 7th Int. Workshop on Stellarators,* Oak Ridge, Tennessee, April 1989, to be published by International Atomic Energy Agency, Vienna (1989).

ORNL/TM-11253
Dist. Category UC-426

INTERNAL DISTRIBUTION

1. C. C. Baker
2. G. L. Bell
3. J. D. Bell
4. L. A. Berry
5. R. D. Benson
6. T. S. Bigelow
7. B. A. Carreras
8. K. KomChipley
9. R. J. Colchin
10. M. J. Cole
11. E. C. Crume
12. R. A. Dory
13. J. L. Dunlap
14. A. C. England
15. R. H. Fowler
16. W. Fulkerson
17. J. C. Glowienka
18. R. H. Goulding
19. J. H. Harris
20. H. H. Haselton
21. D. L. Hillis
22. S. Hiroe
23. L. D. Horton
24. H. C. Howe
25. R. C. Isler
26. T. C. Jernigan
27. R. L. Johnson
28. R. A. Langley
29. M. S. Lubell
30–34. J. L. Lyon
35. M. M. Menon
36. P. K. Mioduszewski
37. R. N. Morris
38. M. Murakami
39. G. H. Neilson
40. B. E. Nelson
41. D. A. Rasmussen
42. J. A. Rome
43. M. J. Saltmarsh
44. D. W. Swain
45. P. B. Thompson
46. M. R. Wade
47. J. A. White
48. T. L. White
49. J. C. Whitson
50. J. B. Wilgen
51. W. R. Wing
52. J. Sheffield
53–54. Laboratory Records Department
55. Laboratory Records, ORNL-RC
56. Central Research Library
57. Document Reference Section
58. Fusion Energy Division Library
59–60. Fusion Energy Division Publications Office
61. ORNL Patent Office

EXTERNAL DISTRIBUTION

62. Office of the Assistant Manager for Energy Research and Development, U.S. Department of Energy, Oak Ridge Operations Office, P. O. Box E, Oak Ridge, TN 37831
63. J. D. Callen, Department of Nuclear Engineering, University of Wisconsin, Madison, WI 53706-1687

64. R. W. Conn, Department of Chemical, Nuclear, and Thermal Engineering, University of California, Los Angeles, CA 90024
65. N. A. Davies, Acting Director, Office of Fusion Energy, Office of Energy Research, ER-50 Germantown, U.S. Department of Energy, Washington, DC 20545
66. S. O. Dean, Fusion Power Associates, Inc., 2 Professional Drive, Suite 248, Gaithersburg, MD 20879
67. H. K. Forsen, Bechtel Group, Inc., Research Engineering, P. O. Box 3965, San Francisco, CA 94119
68. J. R. Gilleland, L-644, Lawrence Livermore National Laboratory, P.O. Box 5511, Livermore, CA 94550
69. R. W. Gould, Department of Applied Physics, California Institute of Technology, Pasadena, CA 91125
70. R. A. Gross, Plasma Research Laboratory, Columbia University, New York, NY 10027
71. D. M. Meade, Princeton Plasma Physics Laboratory, P.O. Box 451, Princeton, NJ 08543
72. M. Roberts, International Programs, Office of Fusion Energy, Office of Energy Research, ER-52 Germantown, U.S. Department of Energy, Washington, DC 20545
73. W. M. Stacey, School of Nuclear Engineering and Health Physics, Georgia Institute of Technology, Atlanta, GA 30332
74. D. Steiner, Nuclear Engineering Department, NES Building, Tibbetts Avenue, Rensselaer Polytechnic Institute, Troy, NY 12181
75. R. Varma, Physical Research Laboratory, Navrangpura, Ahmedabad 380009, India
76. Bibliothek, Max-Planck Institut für Plasmaphysik, Boltzmannstrasse 2, D-8046 Garching, Federal Republic of Germany
77. Bibliothek, Institut für Plasmaphysik, KFA Jülich GmbH, Postfach 1913, D-5170 Jülich, Federal Republic of Germany
78. Bibliothek, KfK Karlsruhe GmbH, Postfach 3640, D-7500 Karlsruhe 1, Federal Republic of Germany
79. Bibliotheque, Centre de Recherches en Physique des Plasmas, Ecole Polytechnique Fédérale de Lausanne, 21 Avenue des Bains, CH-1007 Lausanne, Switzerland
80. R. Aymar, CEN/Cadarache, Departement de Recherches sur la Fusion Contrôlée, F-13108 Saint-Paul-lez-Durance Cedex, France
81. Bibliothèque, CEN/Cadarache, F-13108 Saint-Paul-lez-Durance Cedex, France
82. Library, Culham Laboratory, UKAEA, Abingdon, Oxfordshire, OX14 3DB, England
83. Library, JET Joint Undertaking, Abingdon, Oxfordshire OX14 3EA, England
84. Library, FOM-Instituut voor Plasmafysica, Rijnhuizen, Edisonbaan 14, 3439 MN Nieuwegein, The Netherlands

85. Library, National Institute for Fusion Science, Chikusa-ku, Nagoya 464-01, Japan
86. Library, International Centre for Theoretical Physics, P.O. Box 586, I-34100 Trieste, Italy
87. Library, Centro Richerche Energia Frascati, C.P. 65, I-00044 Frascati (Roma), Italy
88. Library, Plasma Physics Laboratory, Kyoto University, Gokasho, Uji, Kyoto 611, Japan
89. Plasma Research Laboratory, Australian National University, P.O. Box 4, Canberra, A.C.T. 2601, Australia
90. Library, Japan Atomic Energy Research Institute, Naka Fusion Research Establishment, 801-1 Mukoyama, Naka-machi, Naka-gun, Ibaraki-ken, Japan
91. G. A. Eliseev, I. V. Kurchatov Institute of Atomic Energy, P. O. Box 3402, 123182 Moscow, U.S.S.R.
92. V. A. Glukhikh, Scientific-Research Institute of Electro-Physical Apparatus, 188631 Leningrad, U.S.S.R.
93. I. Shpigel, Institute of General Physics, U.S.S.R. Academy of Sciences, Ulitsa Vavilova 38, Moscow, U.S.S.R.
94. D. D. Ryutov, Institute of Nuclear Physics, Siberian Branch of the Academy of Sciences of the U.S.S.R., Sovetskaya St. 5, 630090 Novosibirsk, U.S.S.R.
95. O. S. Pavlichenko, Kharkov Physical-Technical Institute, Academical St. 1, 310108 Kharkov, U.S.S.R.
96. Deputy Director, Southwestern Institute of Physics, P.O. Box 15, Leshan, Sichuan, China (PRC)
97. Director, The Institute of Plasma Physics, P.O. Box 26, Hefei, Anhui, China (PRC)
98. R. A. Blanken, Experimental Plasma Research Branch, Division of Applied Plasma Physics, Office of Fusion Energy, Office of Energy Research, ER-542, Germantown, U.S. Department of Energy, Washington, DC 20545
99. R. A. E. Bolton, IREQ Hydro-Quebec Research Institute, 1800 Montee Ste.-Julie, Varennes, P.Q. JOL 2P0, Canada
100. D. H. Crandall, Experimental Plasma Research Branch, Division of Applied Plasma Physics, Office of Fusion Energy, Office of Energy Research, ER-542, Germantown, U.S. Department of Energy, Washington, DC 20545
101. R. L. Freeman, General Atomics, P.O. Box 85608, San Diego, CA 92138-5608
102. K. W. Gentle, RLM 11.222, Institute for Fusion Studies, University of Texas, Austin, TX 78712
103. R. J. Goldston, Princeton Plasma Physics Laboratory, P.O. Box 451, Princeton, NJ 08543
104. J. C. Hosea, Princeton Plasma Physics Laboratory, P.O. Box 451, Princeton, NJ 08543

105. R. Dagazian, Division of Confinement Systems, Office of Fusion Energy, Office of Energy Research, ER-55, Germantown, U.S. Department of Energy, Washington, DC 20545
106. R. H. McKnight, Experimental Plasma Research Branch, Division of Applied Plasma Physics, Office of Fusion Energy, Office of Energy Research, ER-542, Germantown, U.S. Department of Energy, Washington, DC 20545
107. E. Oktay, Division of Confinement Systems, Office of Fusion Energy, Office of Energy Research, ER-55, Germantown, U.S. Department of Energy, Washington, DC 20545
108. D. Overskei, General Atomics, P.O. Box 85608, San Diego, CA 92138-5608
109. R. R. Parker, Plasma Fusion Center, NW 16-288, Massachusetts Institute of Technology, Cambridge, MA 02139
110. W. L. Sadowski, Fusion Theory and Computer Services Branch, Division of Applied Plasma Physics, Office of Fusion Energy, Office of Energy Research, ER-541, Germantown, U.S. Department of Energy, Washington, DC 20545
111. J. W. Willis, Division of Confinement Systems, Office of Fusion Energy, Office of Energy Research, ER-55, Germantown, U.S. Department of Energy, Washington, DC 20545
112. A. P. Navarro, Division de Fusion, CIEMAT, Avenida Complutense 22, E-28040 Madrid, Spain
113. Laboratory for Plasma and Fusion Studies, Department of Nuclear Engineering, Seoul National University, Shinrim-dong, Gwanak-ku, Seoul 151, Korea
114. J. L. Johnson, Plasma Physics Laboratory, Princeton University, P.O. Box 451, Princeton, NJ 08543
115. L. M. Kovrizhnykh, Institute of General Physics, U.S.S.R. Academy of Sciences, Ulitsa Vavilova 38, 117924 Moscow, U.S.S.R.
116. T. Obiki, Plasma Physics Laboratory, Kyoto University, Gokasho, Uji, Kyoto, Japan
117. A. Iiyoshi, National Institute for Fusion Science, Chikusa-ku, Nagoya 464-01, Japan
118. V. D. Shafranov, I. V. Kurchatov Institute of Atomic Energy, P.O. Box 3402, 123182 Moscow, U.S.S.R.
119. J. L. Shohet, Torsatron/Stellarator Laboratory, University of Wisconsin, Madison, WI 53706
120. G. Grieger, Max-Planck Institut fur Plasmaphysik, D-8046 Garching, Federal Republic of Germany
121. K. Matsuoka, National Institute for Fusion Science, Chikusa-ku, Nagoya 464-01, Japan
122. F. L. Ribe, University of Washington, Aerospace and Energetics Research Program, Mail Stop FL-10, Seattle, WA 98915
123. D. G. Swanson, Auburn University, Department of Physics, Auburn, AL 36849
124. R. K. Linford, Los Alamos National Laboratory, MS F646, P.O. Box 1663, Los Alamos, NM 87545

125. K. I. Thomassen, L-637, Lawrence Livermore National Laboratory, P.O. Box 5511, Livermore, CA 94550

126–176. Given distribution as shown in OSTI-4500, Magnetic Fusion Energy (Category Distribution UC-426)

☆U.S. GOVERNMENT PRINTING OFFICE 1989–648-119/00074